Automotive Radar Multipath Propagation in Uncertain Environments

Alexander Kamann[1], Patrick Held[1], Florian Perras[1], Patrick Zaumseil[1],
Thomas Brandmeier[1] and Ulrich T. Schwarz[2]

Abstract— Future use of high-resolution near range radar sensors for vehicle environment perception is facing challenges in terms of detection and correct assignment of multipath reflections (false-positives) from surfaces and obstacles. This paper presents a novel geometric model to determine the relative positions from surrounding targets and reflection surfaces assuming that every object moves on a circular path to a mutual center. Principles of electromagnetic wave propagation under consideration of incident wave angles at potential reflection surfaces are described. Radar measurements illuminating an experimental target and a highway barrier as reflection surface, which reproducibly generates several multipath reflections, were carried out in a deterministic test environment and validate our presented methods. The installation of absorption material at intense reflection areas was conducted as countermeasure to reduce the intensity of false-positive detections. Furthermore, a realistic urban driving scenario using a real vehicle as target object and a building wall was reconstructed to proof field relevance.

Fig. 1: Driving scenario with ghost object presence.

I. INTRODUCTION

Continuous progress in the development of advanced driver assistance systems (ADAS) leads to an extensive perception of the vehicle environment by imaging sensors. In addition to camera and lidar sensors, radar sensors play a key role in detecting and interpreting the obstacles and free space surrounding the ego-vehicle. Their ability to provide three-dimensional target information consisting of range, relative radial velocity and azimuthal direction determination in poor visibility and weather conditions make them indispensable in addressing the challenges of autonomous driving.

One of these challenges is the type of propagation that the radar signal might take on the transmitting or receiving path. After reflection on an obstacle, the coherently emitted waves of an frequency-modulated continuous-wave radar (FMCW) are subject to multipath propagation [1], [2]. Thus, the radar receives not only the direct reflection of an obstacle, but also indirect temporally shifted reflection components. This superposition can lead to range dependent interference patterns, which cause oscillating signal amplitudes of the received power [3]. In addition to a performance degradation of the direction of arrival (DOA) estimation due to fading effects, multipath propagation can lead to the appearance of

mirrored ghost targets [4]–[6]. Fig. 1 illustrates this effect based on a typical traffic scenario, where the ego-vehicle is being approached by another vehicle from a certain distance along a curved road. The receiving radar signal consists of the corresponding propagation paths including the specular multipath propagation via the guardrail inducing a ghost target with a velocity component directed towards the ego vehicle. In [5], Engels et al. show that the occurrence of ghost targets through multipath reflections in long range applications can lead to an overall deterioration of the sensor performance and creates high demands on signal-processing algorithms with regard to the suppression of mispredictions and thus to false-triggered active security systems. By using a decoupled high resolution frequency estimation method in the Fourier domain, the estimation of the actual target positions, that are subject to multipath propagation, can be significantly increased. However, a detailed analysis of multipath propagation for correct classifications of ghost targets is still of primary importance. Taking into account the current ADAS developments regarding the future use of high-resolution near range radar sensors for the direct vehicle environment with wide field of views, the influence of multipath reflections will increase dramatically. This paper presents a model-based geometric method that demonstrates the occurrence and the behavior of multipath reflections and validates the results with measured data of a custom target and real driving scenarios for various reflection surfaces.

This paper is organized as follows: Section II introduces the propagation principles of electromagnetic waves considering their polarization dependent reflection behavior and

[1]The authors are with the Center of Automotive Research on Integrated Safety Systems and Measurement Area (CARISSMA), Technische Hochschule Ingolstadt, Ingolstadt, Germany. Email: {alexander.kamann, patrick.held, florian.perras, patrick.zaumseil, thomas.brandmeier}@carissma.eu

[2]Ulrich T. Schwarz is with Experimental Sensor Science, Chemnitz University of Technology, Chemnitz, Germany. Email: ulrich.schwarz@physik.tu-chemnitz.de
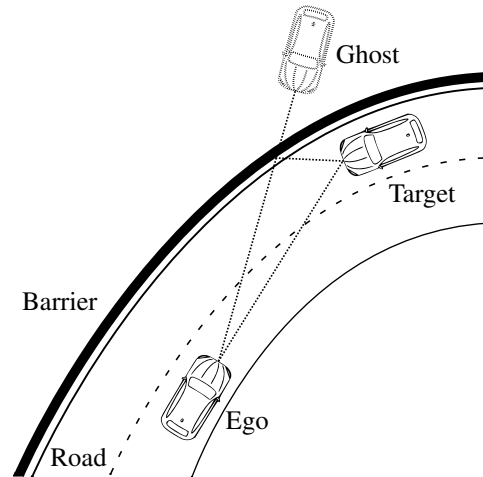
presents the geometric multipath model for determination of the radar wave paths. Section III gives an overview of the chirp sequence modulation and presents the experimental setup. Section IV shows the obtained radar measurements and analyzes the achieved validation results. Finally, Section V summarizes the results and the scientific contribution of this paper and discusses future work.

II. METHODS

A. Electromagnetic Wave Propagation

The isotropic electromagnetic wave propagation in free space between a transmitting and receiving antenna can be modeled by Friis' equations published in [7]. Defining the effective antenna area by

$$A_{eff} = P_r/P_0, \tag{1}$$

where P_r is the power available at the output terminals of the receiving antenna and P_0 is the power flow per unit area of the incident field at the antenna. Considering a setup with an isotropic transmitting antenna and a receiving antenna with effective area A_r, the power flow per unit area at a certain distance d from the transmitter is

$$P_0 = \frac{P_t}{4\pi d^2}, \tag{2}$$

where P_t is power fed into the transmitting antenna at its input terminals. Replacing the isotropic transmitting antenna with a transmitting antenna with effective area A_t will increase the received power by the ratio $A_t/A_{isotr.}$ with $A_{isotr.} = \lambda^2/4\pi$ and we obtain

$$\frac{P_r}{P_t} = \frac{A_r A_t}{d^2 \lambda^2}, \tag{3}$$

where λ is the wavelength. The relation between an antenna gain and the effective antenna area can be described by

$$G_{r,t} = \frac{4\pi}{\lambda^2} A_{r,t}, \tag{4}$$

where G_r is the antenna receiver gain and G_t the antenna transmitter gain. Thus, the received power between a transmitting and receiving antenna in a distance d can be expressed by

$$\frac{P_r}{P_t} = G_r G_t \left(\frac{\lambda}{4\pi d}\right)^2. \tag{5}$$

Assuming an obstacle with radar cross section (RCS) σ at a distance d to the transmit and receive antenna, the reflection is given by

$$\frac{P_r}{P_t} = G_r G_t \left(\frac{\lambda^2}{(4\pi d)^2}\right)^2 \left(\frac{4\pi\sigma}{\lambda^2}\right). \tag{6}$$

B. Reflection

In real world environments, where e.g. buildings, other vehicles or barriers are present, the transmitted energy gets either absorbed, transmitted through the material, reflected (specular reflection) or scattered. The polarization is defined as either parallel or orthogonal to the reflection plane generated by the direction of incidence and reflection. For
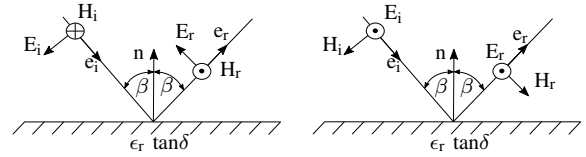

Fig. 2: Reflection geometry and orientation definition of electric field strength of an incident and reflected plane wave for parallel (left) and orthogonal (right) polarization.

parallel polarization the incident radiation where the E-field is oriented parallel to the plane of incidence and for perpendicular polarization the E-field is perpendicular to plane of incidence. For vertical obstacle surfaces, e.g. other cars or walls, horizontal polarization is parallel to the plane of incidence while vertical polarization is perpendicular. The geometric relations are shown in Fig. 2. The reflection coefficient depends on conductivity, angle of incidence, permittivity and roughness of the surface and the polarization of the incident wave

$$R = R_s \cdot \rho, \tag{7}$$

where R is the general reflection coefficient, R_s is the smooth surface reflection coefficient and ρ is the scalar surface roughness attenuation factor. $R_{s\parallel}$ and $R_{s\perp}$ is given by the Fresnel equations

$$R_{s\parallel} = \frac{\sin\beta - \sqrt{\epsilon - \cos^2\beta}}{\sin\beta + \sqrt{\epsilon - \cos^2\beta}}, \tag{8}$$

$$R_{s\perp} = \frac{\epsilon\sin\beta - \sqrt{\epsilon - \cos^2\beta}}{\epsilon\sin\beta + \sqrt{\epsilon - \cos^2\beta}}, \tag{9}$$

where β is the angle of incidence and ϵ is the complex permittivity given by

$$\epsilon = \epsilon_0\epsilon_r - j\frac{\sigma}{\omega}, \tag{10}$$

where ϵ_r is the relative dielectric constant, σ the conductivity of the reflecting surface and ω the angular frequency. The roughness attenuation factor for ρ is given in [8] as

$$\rho^2 = e^{-2\delta}, \text{ with } \delta = \frac{4\pi\Delta h}{\lambda}\sin\beta, \tag{11}$$

where Δh is the standard deviation of the normal distribution for the surface roughness. In real world environments the particular roughness features are usually vaguely known and depend on obstacles geometries.

The power density at the reflection surface is computed and then multiplied by σ of the surface to yield the total scattered power from the surface. The scattering coefficient is given in [9] as

$$A_{scat} = \frac{\sigma}{4\pi d_s^2}, \tag{12}$$

where d_s is the distance from the scatterer to the receiver or another obstacle. When an electromagnetic wave gets reflected at an obstacle the power P_r in (6) gets multiplied by A_{scat} and the reflection coefficient in (7), which yields the received power at the sensor.

C. Geometric Multipath Propagation Model

Fig. 3 shows the multipath reflections that occur on a given reflection surface between a radar sensor and a target object at sensor height. The electromagnetic wave emitted by the sensor is reflected by an object and is subject to multipath propagation. Consequently, the receiving radar signal represents a superposition of four propagation paths, whose frequency components assign different distances. This leads to the occurrence of false-positive reflections (O_{FPn}). Hence, sensor perception of the vehicle environment, based on forward-looking sensors, contains non-existing obstacles which can lead to fatal real world driving situations for humans and vehicles in future automated driving scenarios. A geometric multipath propagation model was developed to determine the radar wave paths. The sensor S (coordinate system origin) travels on a circular path with radius $\vec{r}_m$ relative to a center point M and spans an angle ψ between the sensor S and the target position T. The electromagnetic wave gets reflected in reflection point P_{ref} at a distance $|\vec{r}_{ref}|$ relative from center point M and angle $\psi/2$. The distance between the target position T and the center point M is $|\vec{r}_t|$. For given M, target object radius $|\vec{r}_t|$, reflection point radius $|\vec{r}_{ref}|$ and angle ψ, the target position T and the reflection point position P_{ref} can be determined using

$$\vec{r}_t = -\hat{r}_m \cdot \boldsymbol{X}_{\text{rot}}^{\psi} \cdot |\vec{r}_t| + \vec{r}_m, \tag{13}$$

$$\vec{r}_{ref} = -\hat{r}_m \cdot \boldsymbol{X}_{\text{rot}}^{\frac{\psi}{2}} \cdot |\vec{r}_{ref}| + \vec{r}_m, \tag{14}$$

where $\boldsymbol{X}_{\text{rot}}^{\alpha}$ is a rotation matrix that rotates a given vector by a clockwise angle α and $\hat{r}_m$ is the normalized vector.
One target object T in the radar field of view causes three false-positive objects $O_{FP\ 1-3}$ due to multipath reflections. The target object reflection is the direct line-of-sight (LOS) reflection. False-positive object $O_{FP\ 1}$ path origins from the sensor to reflection surface, gets reflected towards the target object and back to the sensor. False-positive object $O_{FP\ 2}$ is the same path backwards. False-positive object $O_{FP\ 3}$ path starts at the sensor, gets reflected towards the target object, back to the reflection surface and back to the sensor leading to the faraway one. The azimuth angles spanned by $\angle(\vec{r}_m, \vec{r}_a)$ and $\angle(\vec{r}_m, \vec{r}_T)$, referred to as δ and γ, can be computed using vector analysis. The wave's travel paths $|\vec{r'}_T|$ and $|\vec{r}_{FP\ 1-3}|$ can be determined using (13) and (14)

$$|\vec{r'}_T| = 2 \cdot (\underbrace{|\vec{r}_t - \vec{r}_m|}_{|\vec{r}_T|}), \tag{15}$$

$$|\vec{r}_{FP\ 1,2}| = \underbrace{|\vec{r}_{ref} - \vec{r}_m|}_{|\vec{r}_a|} + |\vec{r}_T| + \underbrace{|\vec{r}_t - \vec{r}_{ref}|}_{|\vec{r}_c|}, \tag{16}$$

$$|\vec{r}_{FP\ 3}| = 2 \cdot (|\vec{r}_a| + |\vec{r}_c|), \tag{17}$$

where $|\vec{r'}_T|$ is the propagation path length from the sensor to the target object and back, whereas $|\vec{r}_{FP\ 1-3}|$ are the path lengths from the sensor to the false-positive detections and back, respectively. The relative false-positive object positions can be determined as vectors using (16), (17) and considering relative azimuth angles δ and γ when the electromagnetic
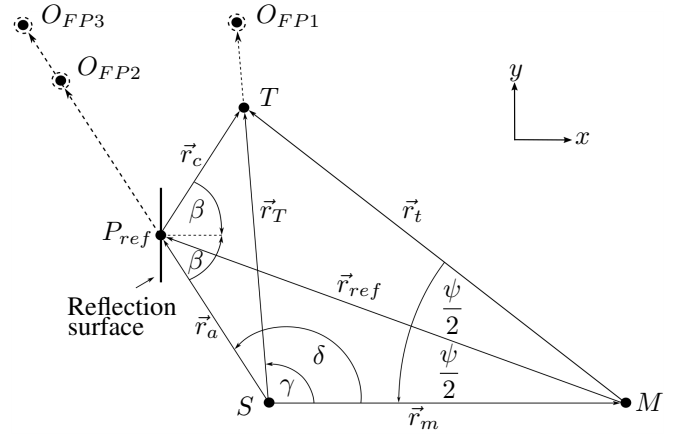

Fig. 3: Multipath propagation model showing a radar sensor (S), a reflection point (P_{ref}) on a reflection surface, a target obstacle (T) and three false-positive reflections ($O_{FP\ 1-3}$).

waves gets reflected back to the sensor either from the reflection point or by the target object using

$$\vec{O}_{FP\ 1} = \vec{e}_x \cdot |\vec{r}_{FP\ 1}| \cdot \boldsymbol{X}_{\text{rot}}^{-\gamma}, \tag{18}$$

$$\vec{O}_{FP\ 2} = \vec{e}_x \cdot |\vec{r}_{FP\ 2}| \cdot \boldsymbol{X}_{\text{rot}}^{-\delta}, \tag{19}$$

$$\vec{O}_{FP\ 3} = \vec{e}_x \cdot |\vec{r}_{FP\ 3}| \cdot \boldsymbol{X}_{\text{rot}}^{-\delta}, \tag{20}$$

where $\vec{e}_x$ is the unit vector in x-direction.

III. EXPERIMENTAL SETUP

A. FMCW Radar Principles & Sensor Parameters

The used $77\,\text{GHz}$-FMCW radar operates by transmitting successive frequency modulated ramps (chirps) with a bandwidth B and a sweep duration T [10]–[12].

$$S_T(t_n) = e^{j2\pi\left(f_c t_n + \nu t_n^2\right)}, \quad t_n \in [0, T], \tag{21}$$

where f_c is the carrier frequency and $\nu = B/(2T)$ represents half the slope of the chirp. Assuming a moving target, in a distance R with constant relative velocity v, corresponds to radar two-way propagation delay of $\tau = 2(R + v t_n)/c$, where c is the speed of light. The time delayed reflection $S_T(t_n - \tau)$ with $\tau << T$ is then down converted to the baseband and low-pass filtered. Thus, the resulting intermediate frequency signal (IF) of one chirp is

$$S_{IF}(t_n) = \xi e^{j2\pi\left(\frac{2f_c R}{c} + \left(\frac{4\nu R}{c} + \frac{2f_c v_r}{c}\right)t_n + \frac{4\nu v_r}{c}t_n^2\right)}, \tag{22}$$

where v_r is the radial projection of v and ξ expresses an amplitude factor considering the occuring attenuation. The last term of (22) is called Range-Doppler-Coupling and can be neglected [10]. The generated beat frequency f_b results in

$$f_b = \underbrace{\frac{4\nu R}{c}}_{f_R} + \underbrace{\frac{2f_c v_r}{c}}_{f_D}. \tag{23}$$

The first term describes the frequency component according to the propagation delay, whereas the second term is the Doppler shift. For assumed large ν values, the frequency term is dominated by $4\nu R/c$. The IF-signal for a series of

N transmitted chirps within a coherent processing interval T_{CPI} appears as a 2-D-array with a time variable $t = n \cdot T_{PRI} + t_n$ consisting of two separate indices t_n and n, where $t_n \in [0,T]$ is the duration of the n-th chirp, whereas $n \in [0, N-1]$ determines the time variable from chirp to chirp within T_{CPI} and is consequently given for a single target scenario by

$$S_{IF}(t_n,n) = \xi e^{j2\pi(\alpha+f_D nT_{PRI}+(f_D+f_R)t_n)}, \qquad (24)$$

with $\alpha = 2f_c R/c$ as a constant phase term. The use of an uniform linear antenna array (ULA) enables the evaluation of the phase progression across L receiving antenna elements with spacing $d_a = c/2f_c$ and thus, the estimation of the azimuthal angular location (R,ϕ) of a target in the spatial domain. The extension of τ by an additional round-trip time delay term $f_c l d_a \sin(\phi)/c$, with $l = 1,\ldots,L$ as the corresponding receiver antenna variable, yields to a three-dimensional complex radar signal of a superposition of K targets given by

$$S_{IF}(t_n,n,l) = \sum_{k=1}^{K} \chi e^{j2\pi(\frac{f_c d_a \sin(\phi_k)}{c}(l-1))}, \qquad (25)$$

$$\text{with } \chi = \xi_k e^{j2\pi(\alpha_k + f_{D_k}nT_{PRI} + (f_{D_k}+f_{R_k})t_n)}.$$

By applying three orthogonal discrete Fourier transformations along the variables t_n, n and l the frequencies corresponding to the range dimension, relative velocity dimension and angular dimension can be estimated.

The INRAS RadarLog is used to carry out the radar measurements. The radar has a ULA frontend with 2 transmit and 16 serial fed patch receive antennas. The frequency resolution in the angular dimension, which is $\arcsin(1/\kappa L d_a)$ with κ as wavenumber, is limited by the number of receiving antennas. To overcome the low resolution of the angular periodogram a high-resolution autoregressive power spectral density technique is applied. Burg's method estimates the partial correlation coefficients by minimizing the average of the forward and backward linear prediction error of the discrete complex radar signals [13]. This removes the sidelobe phenomena of the periodogram and produces high resolution estimates. The high angular resolution together with a used bandwidth of 2 GHz leading to a range gate length of 0.075 m enable the separation ability of the occuring reflections and provide a detailed analysis of the resulting false-positives. The raw data processing of the sampled IF-signals is done in MATLAB.

B. Experimental Setup

Radar sensor measurements with a custom target, a real vehicle and a barrier were conducted to test and validate the presented model. The experimental setup is shown in Fig. 4. The radar sensor is placed stationary with an angle $\alpha = 45°$ rotated towards the reflection surface representing a future automotive corner radar. The custom target consists of 2 trihedral retroreflectors and a metal plate. One retroreflector causes a direct reflection back to the sensor and the other one reflects the wave, coming from the reflection surface,
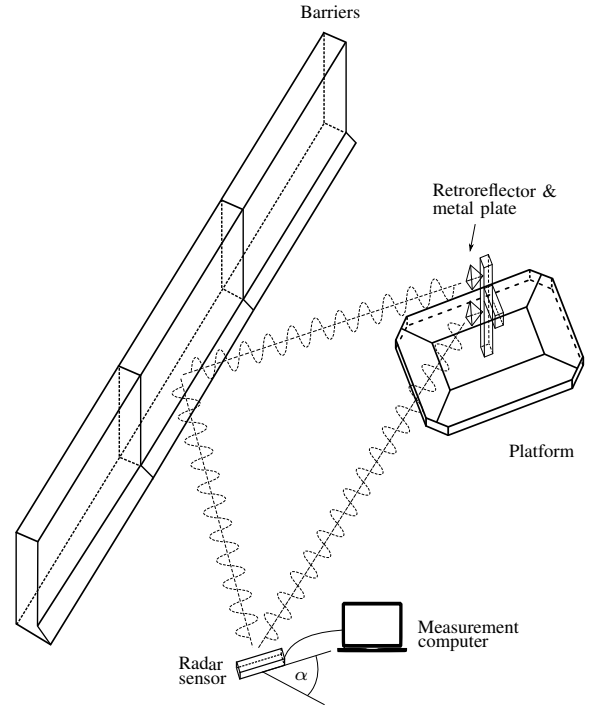

Fig. 4: Experimental configuration showing the radar sensor, a barrier and the target object on a platform.

back to the barrier leading to false-positive object 3 in Fig. 3. The metal plate represents a license plate and the front bumper of a real vehicle and generates false-positive target 1 and 2 in Fig. 3. The multipath propagation assumptions made in the model are validated using anechoic panels. The pyramidal shape and the material of the graphite coated polyurethane panels provide a significant attenuation and enable reproducible indoor radar testing. Measurements using the radar, custom target, real barriers and either with or without anechoic panels are carried out. Furthermore, an intersection crossing scenario is reconstructed as real world driving situation using the radar sensor as future corner radar combined with test vehicle. The radar sensor is facing towards a building with an angle of $45°$ in a certain distance (sidewalk width). Another vehicle is crossing the intersection straight and approaching from the left.

IV. RESULTS

Fig. 5 shows radar measurement results according to the described experimental setup in section III-B and the signal processing presented in section III-A as discrete Fourier transformations, respectively. The subfigures show a topview on the x-y plane of the radar's sensor field of view with either the custom target or a real vehicle as present target and either a real barrier or a wall as reflection surface. In the following the relative position of obstacles in the sensor's field of view shall be referred to as cartesian coordinates (x, y). Subfig. 5a shows a single measurement shot illuminating blank barriers and the target obstacle (T). Multipath reflections (marking 1, 2 and 3) from the barrier and the obstacle
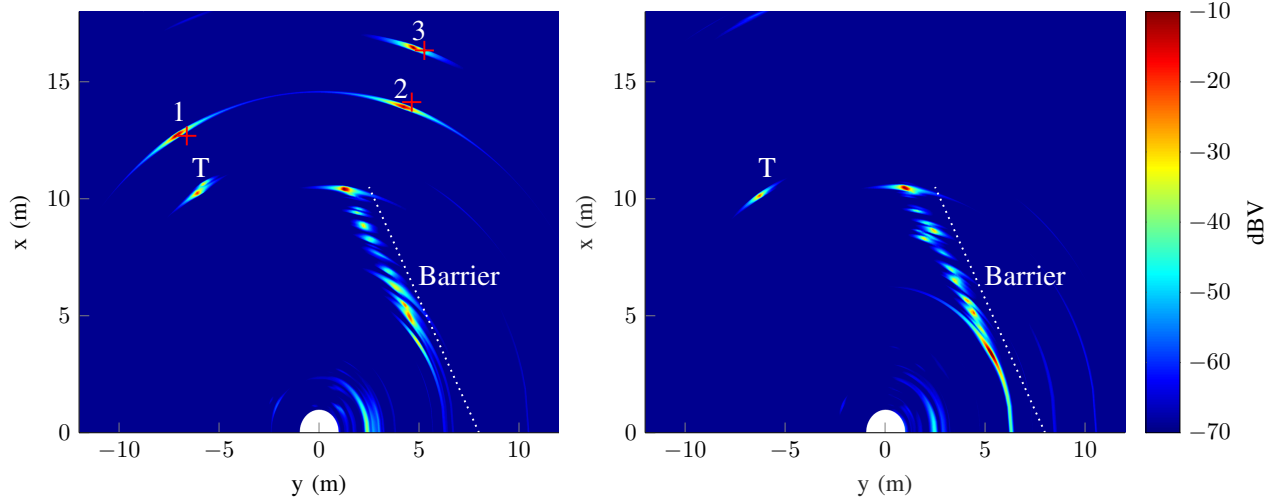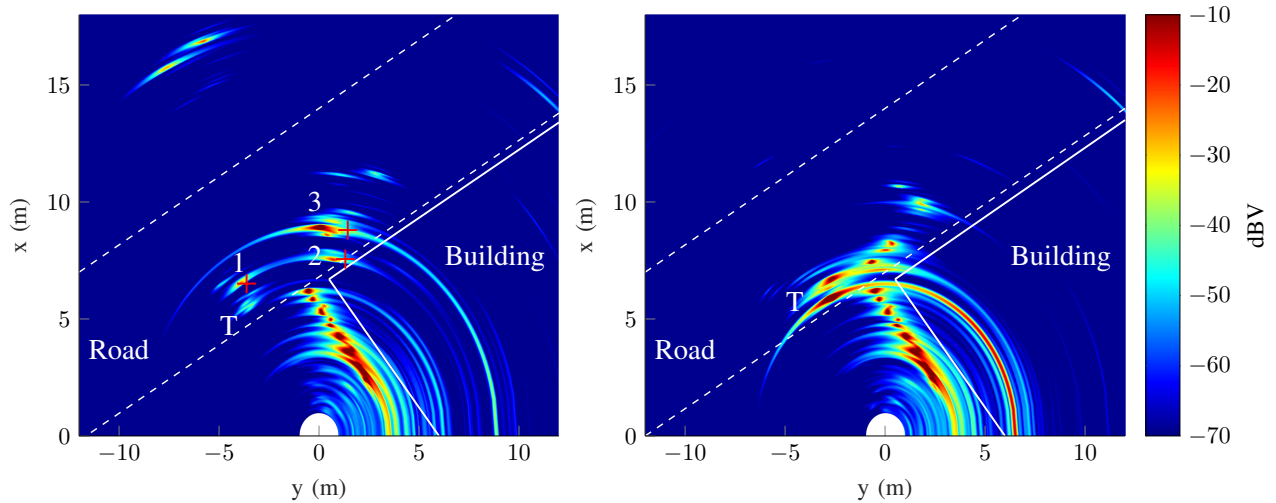
(a) Radar shot with a target (T) and 3 multipath reflections (1-3).

(b) Radar shot with mounted anechoic panels, the target and attenuated multipath reflections.
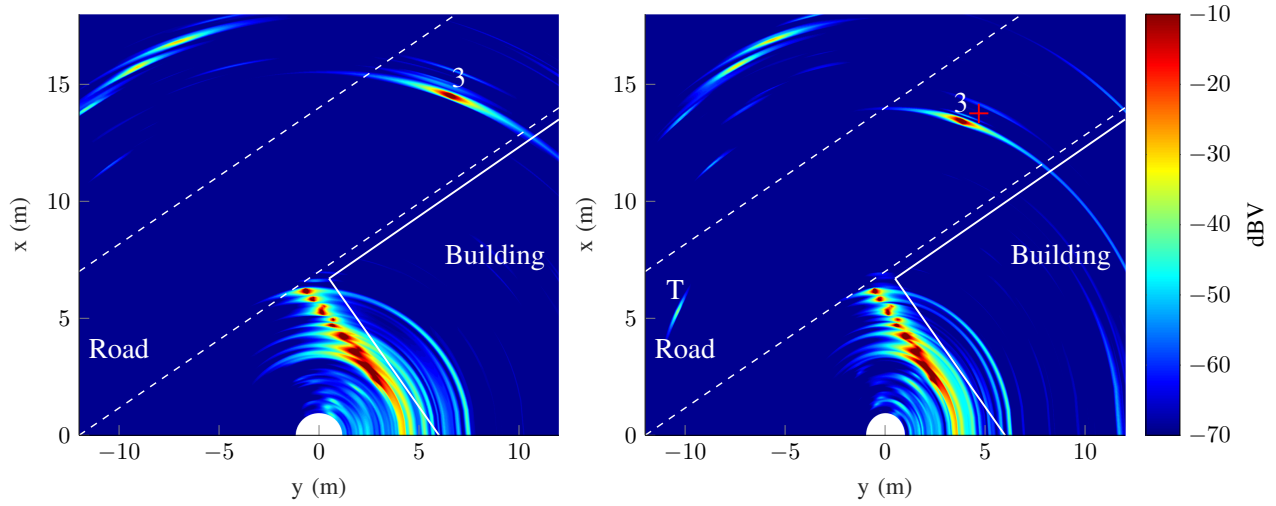
(c) Radar shot with one multipath reflection.

(d) Radar shot with a real vehicle and one multipath reflection.

(e) Radar shot with a real vehicle and all multipath reflections.

(f) Radar shot with a real vehicle and random multipath reflections.

Fig. 5: Radar shot results using a radar sensor, a custom reference target and a real target vehicle.

are clearly visible and appear as stated in section II. The results of our presented model are marked as three red crosses localizing the corresponding false-positive multipath reflections. Subfig. 5b shows a single measurement shot with the same experimental setup illuminating barriers with the direct reflection area covered by anechoic panels and the custom target. The target's direct and barrier reflections are clearly visible, but all multipath reflections are attenuated by installation of several absorption panels. Subfig. 5c shows a building as reflection surface close to the sensor leading to intense reflections and broad peaks. In the up right corner at (6, 14.5) one multipath reflection from the real vehicle as target is shown. It corresponds to multipath reflection 3 from the model. Due to the geometric extension by the vehicle a broader main peak and less intense surrounding peaks are detectable. Due to the 45° rotated radar sensor there is no direct reflection from the target vehicle since the observable target is not yet in the field of view, and hence, undetectable in this early stage of the scenario. In Subfig. 5d both, the target vehicle and one multipath reflection are present. The false-positive reflections show a higher intensity due to the radar sensor's antenna characteristic emitting a higher power in the main lobe and less power in the side lobes. Due to this high power the multipath reflection can be identified as multipath reflection 3 from the model. Subfig. 5e shows the target vehicle, which has further approached to the sensor. The false-positive reflections and the LOS reflection from the vehicle split into multiple intense peaks. Again, the false-positive reflection shows a higher intensity due to the radar sensor's antenna characteristic. The radar sensor illuminates the target vehicle's right side leading to the less intense reflection (T) and simultaneously enables multipath reflections 1, 2 and 3. Due to the close distance from sensor, reflection surface, target vehicle and, in addition, due to the large reflection areas from the building and the target vehicle's side surface, it is highly likely to enable all multipath reflections at the same time in real world driving scenarios. In Subfig. 5f the target vehicle is at the same lateral position as the wall of the building causing an random generation of multipath and direct LOS reflections from the radar sensor to reflection surface and backwards to the sensor. A separation between multipath reflections and the true target vehicle is hardly possible.

V. SUMMARY AND FUTURE WORK

The presented work analyzes the emergence and behavior of radar-based multipath reflections, leading to multiple false-positive targets and an elevated false alarm rate in real world driving scenarios for future use of high-resolution short range radar sensors in the field of vehicle environment perception. The propagation and reflection behavior of electromagnetic waves has been derived and applied to a geometric reflection model illustrating the occurring multipath reflections on real world reflection surfaces, e.g. building walls or road-bounding barriers. An overview of the FMCW radar principle is given, the signal processing of raw sensor data is expressed and applied on raw FMCW radar sensor

data using two DFTs and a high resolution angular algorithm. A novel geometric propagation model describing the relative positions of the false-positive reflections is presented and validated with extensive radar sensor data. The use of an custom reflector target mounted on a platform, creating deterministic point targets as dominant backscatter centers of a vehicle body, validated the different multipath reflections and the overall accuracy of the presented model. Radar measurements of a vehicle during an intersection driving scenario provides detailed insights into the multipath reflection behavior and additionally confirms the assumptions made in the model. The results identify the emerging challenges for the correct interpretation of false-positive targets to enable sophisticated automotive safety-, comfort- and automation applications. Based on these results, further investigations on the effects of multipath reflections for automotive radar sensors need to be carried out to analyze the influence also on the object's velocity determination based on the Doppler effect. First observations show a shifted velocity signature for every false-positive object for varying numbers of reflections.

REFERENCES

[1] H. N. Wang, Y. W. Huang, and S. J. Chung, "Spatial diversity 24-ghz fmcw radar with ground effect compensation for automotive applications," *IEEE Transactions on Vehicular Technology*, vol. 66, pp. 965–973, Feb 2017.

[2] M. Guo, Z. Sun, S. Yang, and Y. Fu, "Genetic algorithm improved spatial diversity 24-ghz fmcw radar with multipath for automotive applications," in *2017 Progress in Electromagnetics Research Symposium - Fall (PIERS - FALL)*, pp. 1988–1993, Nov 2017.

[3] F. Diewald, J. Klappstein, F. Sarholz, J. Dickmann, and K. Dietmayer, "Radar-interference-based bridge identification for collision avoidance systems," in *2011 IEEE Intelligent Vehicles Symposium (IV)*, pp. 113–118, June 2011.

[4] T. Visentin, J. Hasch, and T. Zwick, "Analysis of multipath and doa detection using a fully polarimetric automotive radar," in *2017 European Radar Conference (EURAD)*, pp. 45–48, Oct 2017.

[5] F. Engels, P. Heidenreich, A. M. Zoubir, F. K. Jondral, and M. Wintermantel, "Advances in automotive radar: A framework on computationally efficient high-resolution frequency estimation," *IEEE Signal Processing Magazine*, vol. 34, pp. 36–46, March 2017.

[6] M. Murad, I. Bilik, M. Friesen, J. Nickolaou, J. Salinger, K. Geary, and J. S. Colburn, "Requirements for next generation automotive radars," in *2013 IEEE Radar Conference (RadarCon13)*, pp. 1–6, April 2013.

[7] H. T. Friis, "A note on a simple transmission formula," in *Proceedings of the IRE*, vol. 34, pp. 254–256, May 1946.

[8] K. Chamberlin and R. Luebbers, "An evaluation of longley-rice and gtd propagation models," *IEEE Transactions on Antennas and Propagation*, vol. 30, pp. 1093–1098, Nov 1982.

[9] H. R. Anderson, "A ray-tracing propagation model for digital broadcast systems in urban areas," *IEEE Transactions on Broadcasting*, vol. 39, pp. 309–317, Sep 1993.

[10] V. Winkler, "Range doppler detection for automotive fmcw radars," in *2007 European Microwave Conference*, pp. 1445–1448, 2007.

[11] E. A. Costa and R. B. Chadwick, "Signal processing and range spreading in the fm-cw radar," National Oceanic and Atmospheric Administration Environmental Research Laboratories, May 1984.

[12] S. M. Patole, M. Torlak, D. Wang, and M. Ali, "Automotive radars: A review of signal processing techniques," *IEEE Signal Processing Magazine*, vol. 34, pp. 22–35, March 2017.

[13] J. Burg, "Maximum entropy spectral analysis," *Proc. 37th Meet. Soc. Exploration Geophysicists, IEEE Press*, vol. 37, pp. 34–39, Nov 1978.